Tomographic Full Waveform Inversion for imaging under complex overburden

Guillaume Barnier, Ettore Biondi, and Biondo Biondi

ABSTRACT

Tomographic Full Waveform Inversion (TFWI) is a waveform inversion technique that uses an extended modeling operator, allowing the predicted data to be in phase with the observed data, even when the starting velocity model is inaccurate. While being robust against cycle-skipping issues inherent to Full Waveform Inversion (FWI), it is still poorly understood whether this technique can be efficient in a complex overburden environment. And if so, which type of model extension is the most adequate to predict and capture the complexity of the waveforms such as the ones reflecting off a top-salt boundary. We first present three synthetic examples that illustrate the issues encountered in complex overburden environments. Then, we review the theoretical framework of TFWI and present our code that allows for space and time-lag extensions. Finally, we test for various model extensions to understand which combination manages to better capture the complexity of a wavefield that is reflected from a top-salt boundary.

INTRODUCTION

Producing accurate and high-resolution images of subsalt reflectors is a key challenge for the oil and gas industry. Companies are still looking for ways to reduce processing cycle-time and third-party costs associated with salt-model building. As shown in previous work, there are two major difficulties associated with subsalt imaging. On one hand, the velocity contrast between the salt rock and the surrounding sediments is so high that a slight misinterpretation can create huge time-shifts in the computation of wavefields, which in turn can translate into a total loss of coherency of migrated images (Etgen et al., 2014a,b; Barnier and Biondi, 2015). On the other hand, salt bodies tend to have rugose and complex boundaries (e.g., carapaces and cap rocks) that generate complicated waveforms typically coming from prismatic waves, multiple scattering, and point diffractors. Therefore, predicted data generated from an incorrect salt model will not match the complex recorded waveforms, and standard algorithms will fail to update the salt model efficiently.

To address these issues, we propose to apply the Tomographic Full Waveform Inversion (TFWI) workflow developed by Biondi and Almomin (2014) to improve images of subsalt reflectors. This technique has been shown to be efficient and immune to cycle-skipping in relatively simple overburden environments (Almomin, 2016). The

modeling is based on an extended Born operator that allows the user to linearly predict data while ensuring that they stay in phase with the observed ones, even when the starting model is "far" from the truth. The non-physical energy in the extended axis is slowly reduced during the iterative process until an optimal and "physical" model is found. Since the algorithm requires the energy in the extended axis to be somewhat coherent in order to converge towards the right solution, it is still poorly understood whether it may be successfully applied to subsalt imaging problems (as energy becomes incoherent even in the extended axis). Another problem may arise from the fact that salt boundaries generate such complicated events that even an extended linear modeling operator might have difficulties replicating them.

In this report, we first show three synthetic examples of FWI that illustrate the limitation of this algorithm when applied to more complex overburdens (e.g., models which contain sharp and high-velocity contrast anomalies). We provide a brief theoretical review of TFWI, we present the structure of our code that allows both subsurface offsets (vertical and horizontal) and time-lag extensions. We then test for different combinations of extensions to understand which one is more likely to be adequate for replicating waveforms generated at a salt-sediment interface. Finally, we apply TFWI on a synthetic example that contains an anomaly with a sharp velocity contrast. All optimization and inversion results in this reports were performed using the optimization library developed in Biondi and Barnier (2017).

LIMITATION OF FULL WAVEFORM INVERSION FOR IMAGING UNDER COMPLEX OVERBURDEN

FWI has been proved to be a very useful and accurate tool for velocity model building in relatively simple overburden environments (Shen, 2014). However, its robustness in the context of subsalt imaging is still an active research topic for the oil and gas industry (Williamson et al., 2016; Wang et al., 2015; Lewis et al., 2012). One of the main challenges is that in order to obtain accurate subsalt images, the sharpness of salt boundaries must be captured by our velocity model. Slight errors in their delineation may result in big distortions of the images (Etgen et al., 2014a,b). Moreover, obtaining higher resolution subsalt images requires the use of higher frequency energy, in which case the wavefields will be increasingly more sensitive to small inaccuracies at the salt-sediment interface. Beyond certain frequencies, the extreme velocity contrast at the interface and its rugosity (e.g., canyons and small-scale anomalies) may generate complicated waveforms (e.g., prismatic waves) which are difficult to predict and replicate with our standard linearized modeling operators (based on single scattering assumption). Failing to capture both the sharpness and the shape of the salt interface may cause convergence issues and FWI may fail to produce accurate velocity models.

The first tests we conduct are designed to assess how well we can recover the sharpness of an abrupt boundary in a simple synthetic setup based on Mora (1989), where we introduce a circular homogeneous anomaly in a background containing two

horizontal layers. We show that if the velocity contrast of the anomaly is not too large, its sharpness and its shape can be well recovered. However, if the contrast is too large, FWI converges towards an incorrect solution, even for an elementary example (synthetic, noise-free and using very low frequency energy). Another issue for imaging in the vicinity of complex salt bodies arises from the fact that it is also still unclear how to choose and construct an efficient starting velocity model for FWI. On one hand, starting with a model containing a salt body with very sharp (but inaccurate) boundaries may be inefficient for FWI convergence because it would take many iterations to "move" and re-adjust these sharp boundaries (i.e., the high-wavenumber components of our model) to the correct location. On the other hand, a starting velocity model with "not enough" salt would also be inefficient since the algorithm would spend a lot of iterations building the high velocity contrast between the salt and its surrounding sediments. Therefore, in our third example, we try to illustrate this issue with a synthetic salt basin environment that replicates a typical setup we may encounter in the Gulf of Mexico (GoM). We start with a smoothed version of the true velocity model, and we show that even with very long-offset data (containing diving waves and refracted energy off the top-salt) and very low frequency energy, the algorithm does not converge towards the correct solution.

Recovering a sharp boundary with a small velocity contrast

We apply FWI on a simple synthetic model which consists of one circular anomaly embedded into a two-layer velocity model shown in Figure 1(g), similar to the one proposed in Mora (1989). The velocity contrast between the anomaly and the top-layer is only 10 %, the shape of the anomaly is simple (circular), and data are modeled and inverted using the same acoustic engine. We perform a multi-scale FWI (Bunks et al., 1995), starting from a frequency band of 0.25-7 Hz, up to 0.25-45 Hz. For each frequency band, we perform 40 iterations of FWI. Though not realistic, this test provides an idea of how well we are able to recover a sharp boundary in a "best case scenario" (i.e., with energy at very low frequencies and noise-free data). In our first test, the initial model is the true model without the anomaly. We investigate how the sharp boundary evolves as we increase frequency and if the algorithm converges towards the true solution. We use a finite-difference grid size of $dz = dx = 10$ m. We place sources every 100 m, and receivers every 10 m at the surface. Results are shown in Figures 1(a)-(f), and we can see a good convergence as we increase the frequency content of our data. We extract a 1D velocity profile at $x = 1$ km, and display the results in Figures 2(a)-(f). We stop the inversion process at 45 Hz to avoid numerical dispersion but the inversion could be pursued with higher frequencies and a smaller finite-difference grid size. The interface between the anomaly and the surrounding background is well recovered, which shows that obtaining such sharpness with FWI is theoretically possible.

Figures 3(a)-(c) show the results of a similar multi-scale FWI inversion scheme, but using a constant velocity background (only the top-layer) as initial model. In

this case, we observe (1) a decrease in the sharpness of the anomaly's boundaries (Figure 3(a)) and (2) an ambiguity in the velocity of the first and second layers, especially close to their interface (Figure 3(b)-(c)).

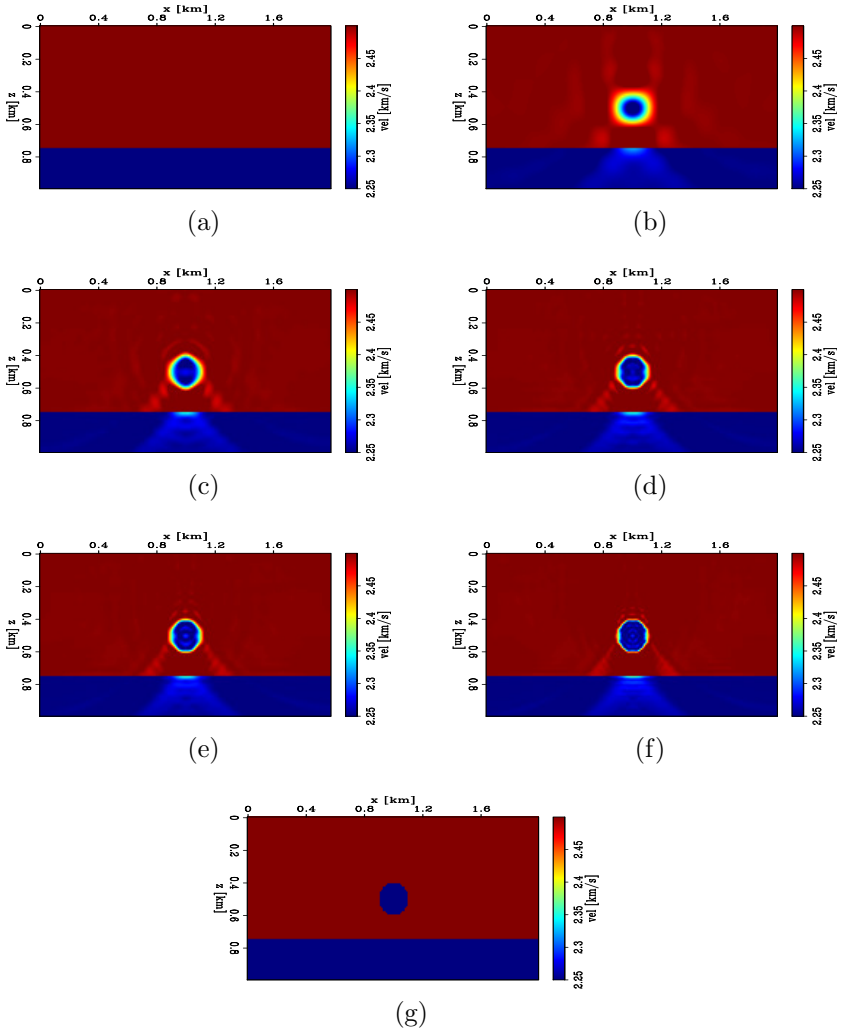

Figure 1: Inverted velocity models using a multi-scale FWI scheme. For each frequency band, we perform 40 iterations of FWI. (a) Initial model. (b) Inverted model using energy up to 7 Hz. (c) Inverted model using energy up to 15 Hz. (d) Inverted model using energy up to 25 Hz. (e) Inverted model using energy up to 30 Hz. (f) Inverted model using energy up to 45 Hz. (g) True model. [**CR**]

Recovering a sharp boundary with a large velocity contrast

We conduct a similar experiment but the velocity contrast between the anomaly and the top-layer is now 125 % (top-layer velocity is 2 km/s and anomaly velocity is 4.5 km/s), which is a typical contrast one can expect when exploring salt basins. Even though we start from a frequency band containing (unrealistic) low-frequency

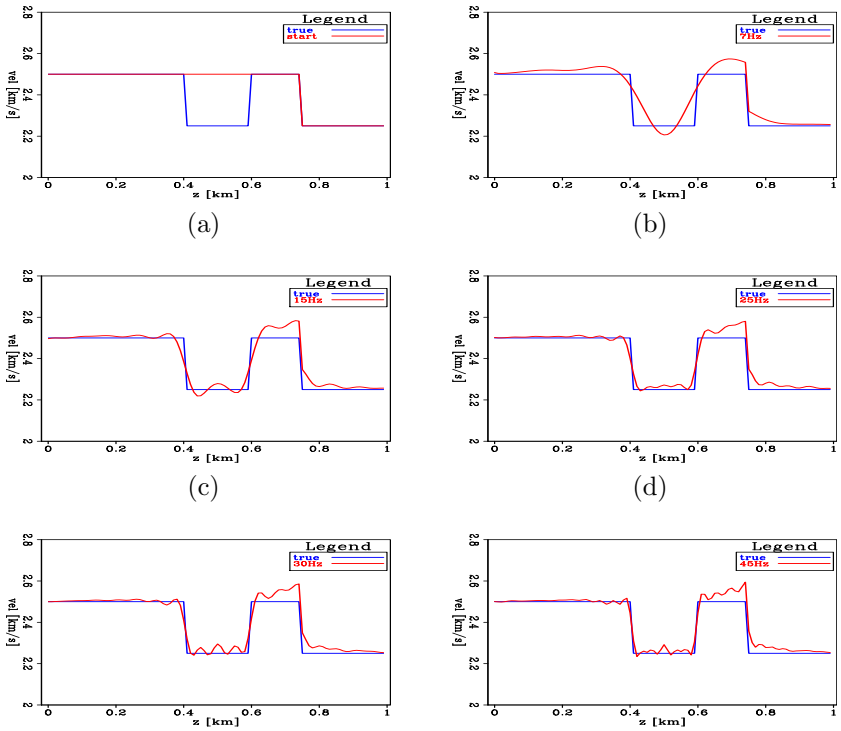

Figure 2: 1D velocity profile of inverted models using a multi-scale FWI scheme extracted at $x = 1$ km. For each frequency band, we perform 40 iterations of FWI. (a) Initial model. (b) Inverted model using energy up to 7 Hz. (c) Inverted model using energy up to 15 Hz. (d) Inverted model using energy up to 25 Hz. (e) Inverted model using energy up to 30 Hz. (f) Inverted model using energy up to 45 Hz. [**CR**]

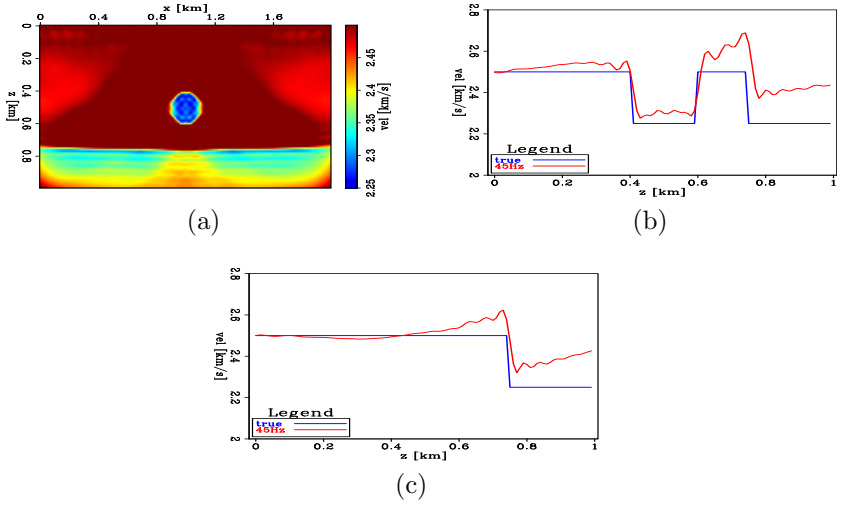

Figure 3: Inverted model with a multi-scale FWI scheme using energy up to 45 Hz and a constant initial velocity model. (a) Full 2D model. (b) 1D profile extracted at $x = 1$ km. (c) 1D profile extracted at $x = 0.4$ km [**CR**]

energy (0.25-5 Hz), the algorithm does not converge towards the correct solution. As in the previous example, we conduct a multi-scale FWI scheme up to 45 Hz. Finite-difference parameters are the same as in the previous example. Results are shown in Figures 4 and 5. For each frequency band, we run 40 iterations of FWI. We can see that the algorithm fails to recover the strong anomaly and its sharp boundaries, even for such a simple setup.

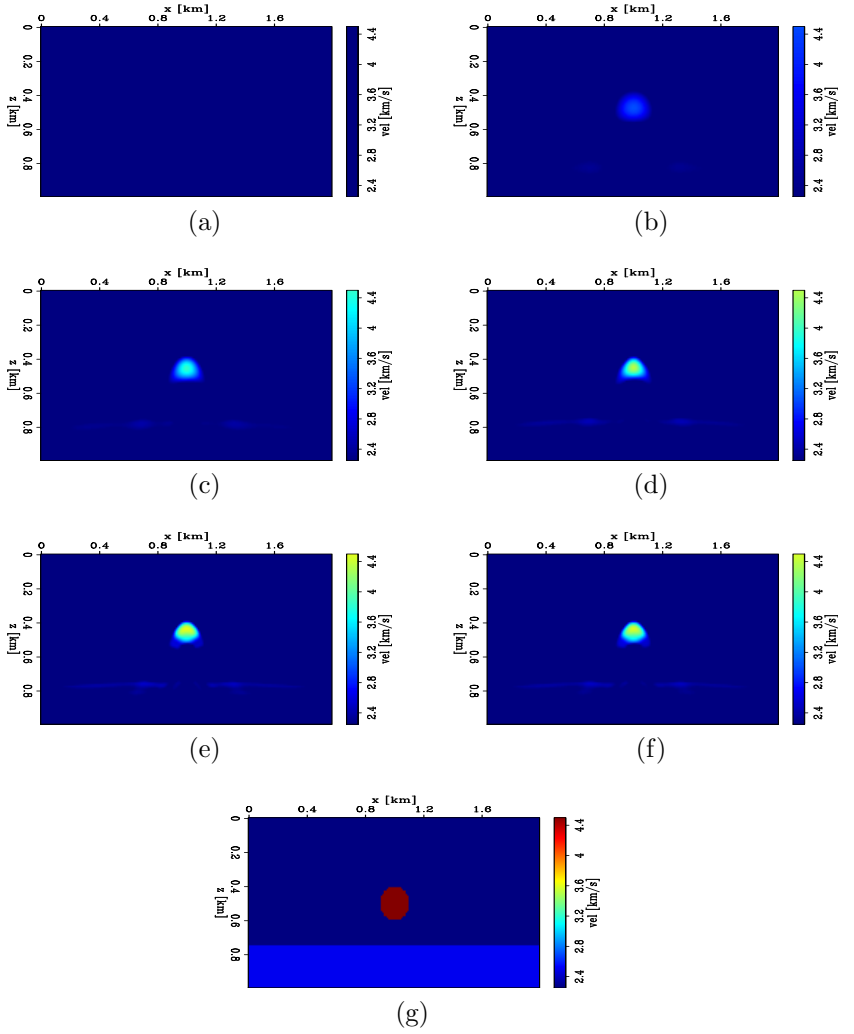

Figure 4: Inverted velocity models using a multi-scale FWI scheme. For each frequency band, we perform 40 iterations of FWI. (a) Initial model. (b) Inverted model using energy up to 5 Hz. (c) Inverted model using energy up to 12 Hz. (d) Inverted model using energy up to 20 Hz. (e) Inverted model using energy up to 30 Hz. (f) Inverted model using energy up to 45 Hz. (g) True model. [**CR**]

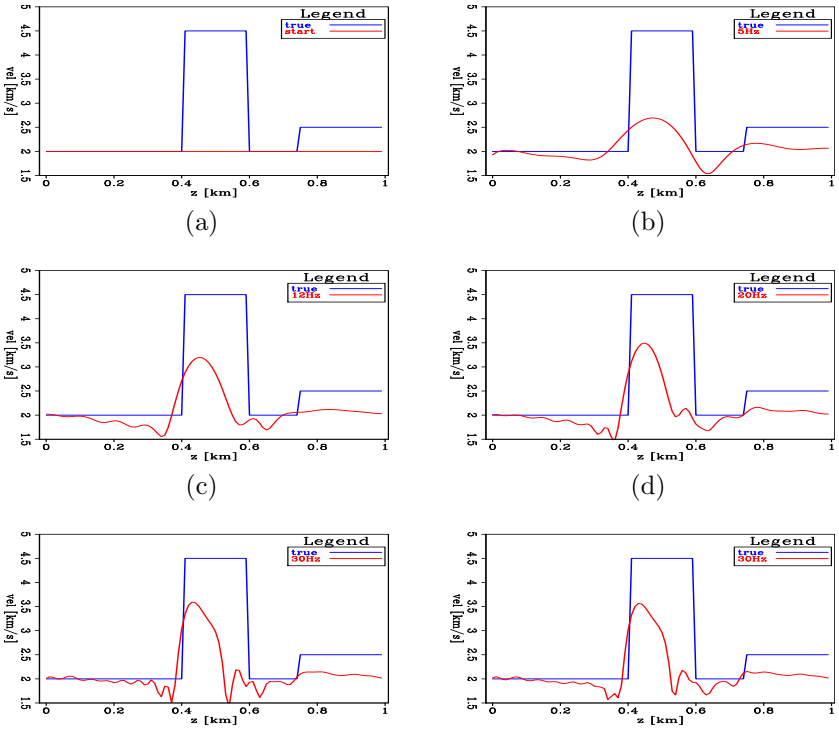

Figure 5: 1D velocity profile of inverted models using a multi-scale FWI scheme, extracted at $x = 1$ km. For each frequency band, we perform 40 iterations of FWI. a) Initial model. (b) Inverted model using energy up to 5 Hz. (c) Inverted model using energy up to 12 Hz. (d) Inverted model using energy up to 20 Hz. (e) Inverted model using energy up to 30 Hz. (f) Inverted model using energy up to 45 Hz. [**CR**]

FWI in the presence of a complex salt body

We apply FWI on a synthetic model that replicates a salt basin environment typically encountered in the GoM. We design our velocity model by combining a sediment model generated using the workflow from Clapp (2014) and by adding a complex salt body (Figure 6(a)). We simulate a long-offset acquisition (20 km), with shots (every 100 m) and receivers (every 10 m) at the surface. Our initial model which was obtained by smoothing the true velocity model, is shown in Figures 6(b)-(c). Figure 7 shows the shot record for a source positioned at $x = 0$ km, containing energy ranging from 0.25 Hz up to 3.5 Hz. In Figure 7, events arriving before the direct arrivals for longer offsets ($x \geq 10$ km) correspond to the refracted energy (traveling almost horizontally through the salt) caused by the high velocity contrast between the salt body and its surrounding sediments. Since the salt body has a rugose top, part of that refracted energy is also scattered and recorded at the surface. We purposely choose to include (unrealistic) low frequencies in our inversion scheme to assess whether the FWI algorithm will able to recover the boundaries of the salt body in the "ideal" case, or at least provide an improved velocity model. We run 30 iterations of FWI and display the results in Figures 8, 9, and 10. Data residuals at various iterations for the shot record generated by a source positioned at $x = 0$ km are shown in Figure 11. Results indicate that most of the updates occur in the shallowest part of the model, and are very small in amplitude (Figure 10(a)-(d)). Even though the top-salt boundary seems be somewhat correctly updated in some areas, we are already starting to see wrong updates just above the salt body (incorrect low velocity zones), which may indicate possible cycle-skipping. Therefore, the salt body boundaries are not being sharpened throughout the inversion process (or updated in the right direction), and the overlying sediments seemed to be wrongly updated in some locations, as seen in Figure 10(d). Future steps include performing a FWI scheme using a higher frequency content.

TOMOGRAPHIC FULL WAVEFORM INVERSION

Almomin (2016) showed that TFWI can be robust and immune to cycle-skipping in relatively simple overburdens, but it is still unclear whether it can be applied to targets located under complex overburdens such as salt bodies. We identified two potential issues that may cause the algorithm to fail. (1) TFWI uses an extended Born modeling operator combined with an extended velocity model which allows the predicted data to stay in phase with the observed ones. The non-physical energy in the extended axis of the velocity model is slowly reduced during the inversion process. However, it requires this energy to be coherent in order to perform efficient tomographic updates to the model. Unfortunately, Etgen et al. (2014a,b); Barnier and Biondi (2015) showed that subsalt images are very sensitive to errors in the salt boundary delineation and rapidly lose coherency even in the extended space. (2) Salt bodies may have complex shapes, especially in the vicinity of the salt-sediments interface (e.g., impedance contrast solely due to a density change, carapaces and canyons). These structures can generate wavefields and wavepaths of such a complexity (e.g., prismatic waves, diffractions

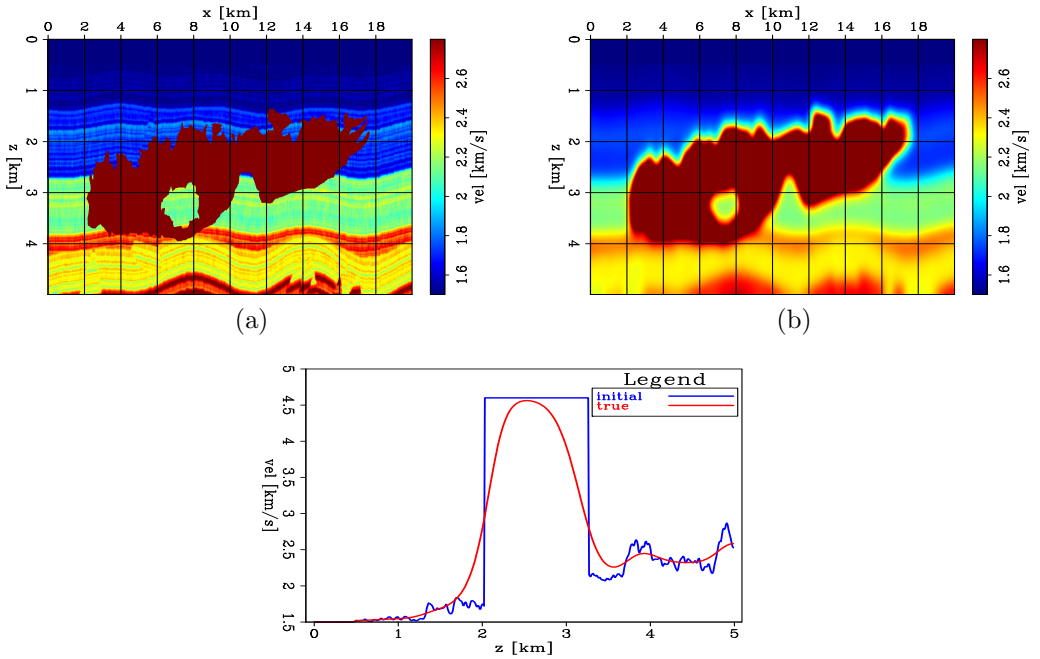

Figure 6: (a) True velocity model. (b) Initial velocity model. (c) 1D profile of the true and initial velocity models extracted at $x = 10$ km. [**NR**]

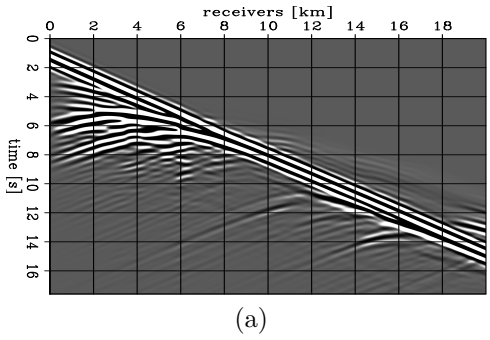

Figure 7: Shot record generated by a source located at $x = 0$ km offset. [**ER**]

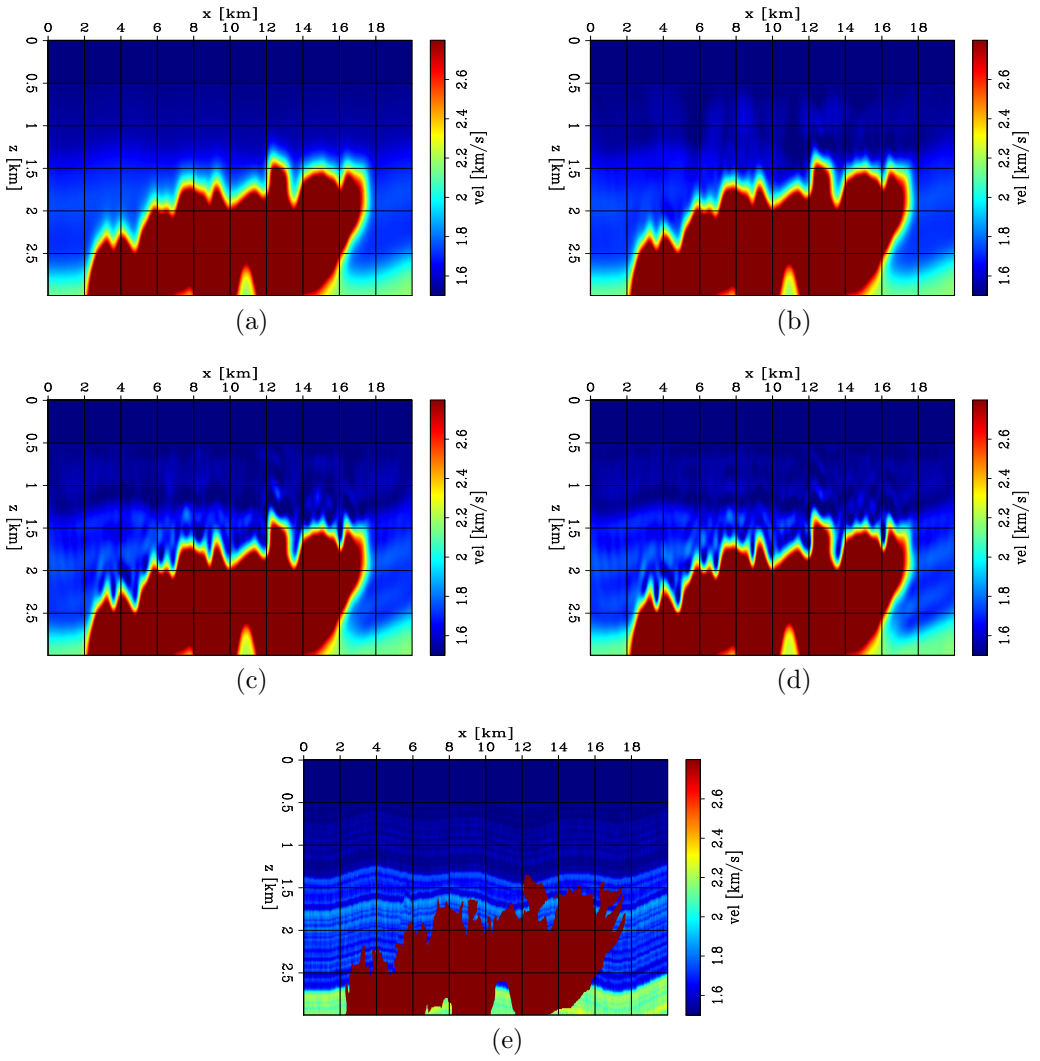

Figure 8: Inverted models at various iterations of the FWI workflow. (a) Starting model. (b) Model after 5 iterations. (c) Model after 15 iterations. (d) Model after 30 iterations. (e) True model. [**ER**]

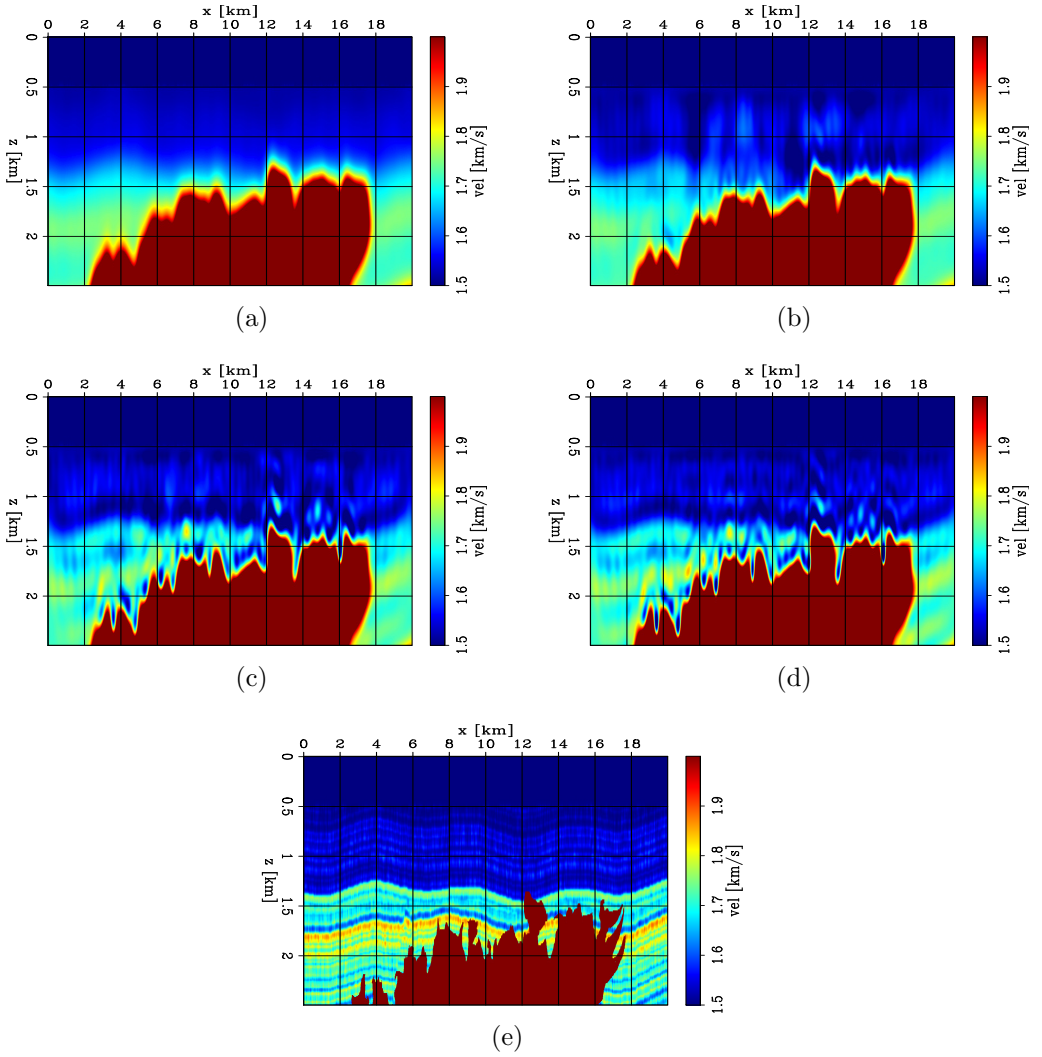

Figure 9: Inverted models at various iterations of the FWI workflow. Figures correspond to the same ones as in Figures 9 but have been clipped to a lower value in order to better show the updates made by the FWI scheme. (a) Starting model. (b) Model after 5 iterations. (c) Model after 15 iterations. (d) Model after 30 iterations. (e) True model. [**CR**]

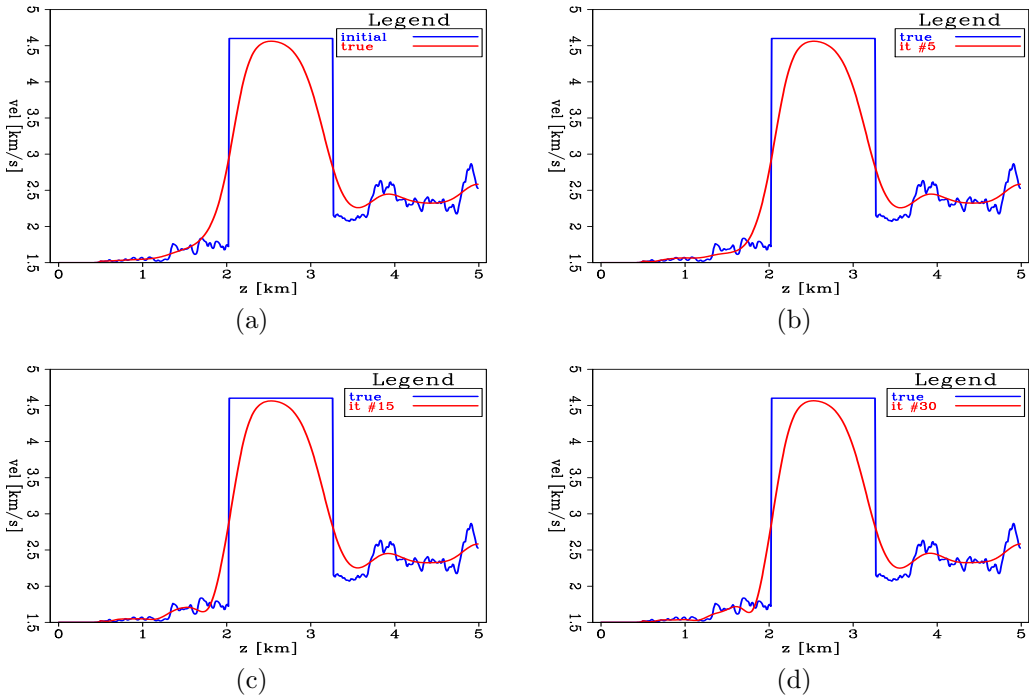

Figure 10: 1D velocity profiles of the inverted models at various iterations of the FWI workflow extracted at $x = 10$ km. (a) Starting model. (b) Model after 5 iterations. (c) Model after 15 iterations. (d) Model after 30 iterations. [**CR**]

and wavefield triplications) that our extended modeling operator may not be able to capture.

We first provide a brief theoretical review of TFWI, we apply the algorithm on the synthetic example shown in the previous section where we try to recover a sharp boundary with large velocity contrast, and we design a test to assess which combination of model extensions are more efficient at replicating wavefields generated by a complex top-salt interface.

Theoretical review

TFWI aims at minimizing the following objective function,

$$\Phi(\tilde{\mathbf{m}}) = \frac{1}{2}\|\tilde{\mathbf{f}}(\tilde{\mathbf{m}}) - \mathbf{d}^{\mathbf{obs}}\|_2^2 + \frac{\epsilon^2}{2}\|\mathbf{A}\tilde{\mathbf{m}}\|_2^2, \tag{1}$$

where $\tilde{\mathbf{m}}$ is the extended velocity model, $\tilde{\mathbf{f}}$ is an extended wave-equation modeling operator, $\mathbf{d}^{\mathbf{obs}}$ are the observed data, and $\mathbf{A}$ is an operator that enhances the non-physical energy of the extended model (e.g., differential semblance optimization

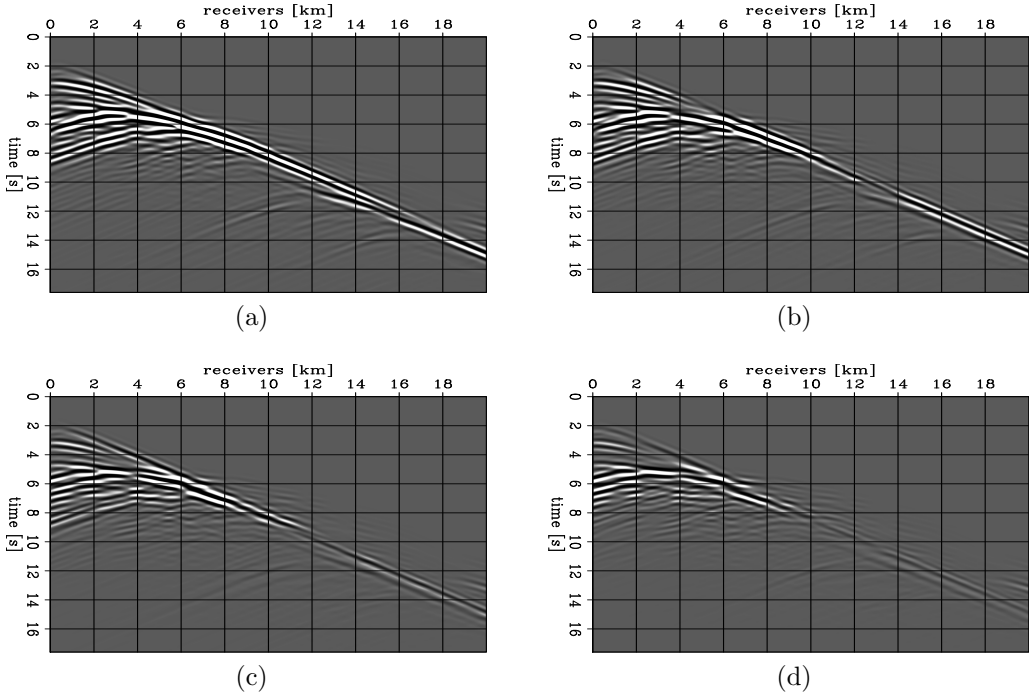

Figure 11: Data residuals for the shot record generated with a source positioned at $x = 0$ km at various iterations of the FWI workflow. (a) Initial residual. (b) Residual after 5 iterations. (c) Residual after 15 iterations. (d) Residual after 30 iterations. [**CR**]

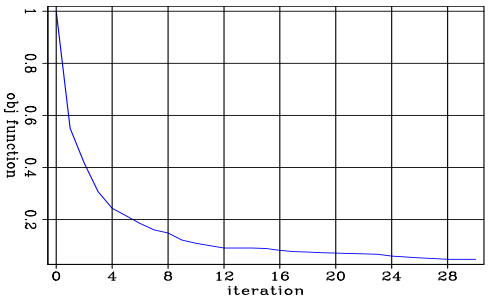

Figure 12: FWI objective function with iteration. [**ER**]

(DSO)). The various types of model extensions are discussed in the next section. The first term of the objective function ensures that our predicted data match the observed ones, while the second term reduces the non-physical energy of our model. Due to computational limitation, modeling wavefields with the extended wave-equation operator $\tilde{\mathbf{f}}$ is impractical, and we linearize our forward modeling operator using the following Born approximation,

$$\tilde{\mathbf{f}}(\tilde{\mathbf{m}}) \approx \tilde{\mathbf{f}}(\tilde{\mathbf{m}}_\mathbf{0}) + \tilde{\mathbf{B}}(\tilde{\mathbf{m}}_\mathbf{0})\Delta\tilde{\mathbf{m}}, \tag{2}$$

where $\tilde{\mathbf{m}}_\mathbf{0}$ is an arbitrary model point, and $\tilde{\mathbf{B}}$ is an extended Born modeling operator, linear with respect to $\Delta\tilde{\mathbf{m}} = \tilde{\mathbf{m}} - \tilde{\mathbf{m}}_\mathbf{0}$. If we choose $\tilde{\mathbf{m}}_\mathbf{0}$ to be non-extended, we now have $\tilde{\mathbf{f}}(\tilde{\mathbf{m}}_\mathbf{0}) = \mathbf{f}(\mathbf{m}_\mathbf{0})$, which is a standard (non-extended) wave-equation propagation. As done in Almomin (2016), we perform a scale separation, where the extended model is divided into two components,

1. a low wavenumber part $\tilde{\mathbf{b}}$ referred to as "background", which is responsible for the kinematic effects (transmissions) of the wavefields, and
2. a high wavenumber part $\tilde{\mathbf{p}}$ referred to as "perturbation", which affects reflected and scattered energy.

Due to high computational costs, the background component is reduced to a non-extended model (while the reflectivity stays extended), and the total model can therefore be expressed by

$$\tilde{\mathbf{m}} \approx \mathbf{b} + \tilde{\mathbf{p}}, \tag{3}$$

where $\mathbf{b}$ is the non-extended background and $\tilde{\mathbf{p}}$ is the extended perturbation. We can re-formulate our forward modeling operator (equation 2) into the form

$$\tilde{\mathbf{f}}(\tilde{\mathbf{m}}) \approx \mathbf{f}(\mathbf{b}) + \tilde{\mathbf{B}}(\mathbf{b})\tilde{\mathbf{p}}. \tag{4}$$

equation 1 becomes

$$\Phi(\tilde{\mathbf{m}}) = \Phi(\mathbf{b}, \tilde{\mathbf{p}}) = \frac{1}{2}\|\mathbf{f}(\mathbf{b}) + \tilde{\mathbf{B}}(\mathbf{b})\tilde{\mathbf{p}} - \mathbf{d}^{\mathbf{obs}}\|_2^2 + \frac{\epsilon^2}{2}\|\mathbf{A}\tilde{\mathbf{p}}\|_2^2. \tag{5}$$

As explained in Almomin (2016), we now invert for two parameters ($\mathbf{b}$ and $\tilde{\mathbf{p}}$) that need to interact with each other in order to maintain a simultaneous inversion of

scales, and both models need to be eventually combined into one physical model that can predict the recorded data. Almomin (2016) proposes a nested scheme composed of an outer and inner loop, described by the following workflow:

iterate outer loop
{
- compute data for inner loops: $\tilde{\mathbf{d}} = \mathbf{d^{obs}} - \mathbf{f(b)}$
- initialize the extended perturbation to zero: $\tilde{\mathbf{p}} = \mathbf{0}$
- iterate inner loop
{
. set $\mathbf{r_d} = \tilde{\mathbf{B}}(\mathbf{b})\tilde{\mathbf{p}} - \tilde{\mathbf{d}}$
. set $\mathbf{r_m} = \mathbf{A}\tilde{\mathbf{p}}$
. set $\tilde{\Phi}(\mathbf{b}, \tilde{\mathbf{p}}) = 0.5\,\|\mathbf{r_d}\|_2^2 + 0.5\,\epsilon^2\|\mathbf{r_m}\|_2^2$
. compute $\nabla_{\mathbf{b}}\tilde{\Phi}$
. compute $\nabla_{\tilde{\mathbf{p}}}\tilde{\Phi}$
. apply scale mixing on both gradients to compute search direction
. apply nonlinear stepper
}
- extract the non-extended component of the perturbation: $\mathbf{p_{ne}}$
- update the background model: $\mathbf{b} \leftarrow \mathbf{b} + \mathbf{p_{ne}}$
- apply a low-wavenumber pass filter on $\mathbf{b}$
}

The data $\tilde{\mathbf{d}}$ are computed once for each outer loop iteration and serve as "observed data" for the inner loops. The gradient with respect to the background model $\nabla_{\mathbf{b}}\tilde{\Phi}$ is given by

$$\nabla_{\mathbf{b}}\tilde{\Phi} = \mathbf{T}^*\mathbf{r_d}, \tag{6}$$

where $\mathbf{T}^*$ is the adjoint tomographic operator defined in Almomin (2016). The extended gradient with respect to the extended perturbation $\nabla_{\tilde{\mathbf{p}}}\tilde{\Phi}$ is given by,

$$\nabla_{\tilde{\mathbf{r}}}\tilde{\Phi} = \tilde{\mathbf{B}}^*\mathbf{r_d} + \epsilon\mathbf{A}^*\mathbf{r_m}, \tag{7}$$

where $\tilde{\mathbf{B}}^*$ denotes the adjoint extended Born modeling operator. It is assumed here that $\mathbf{A}$ is a linear operator with respect to $\tilde{\mathbf{p}}$. After computing both gradients (at each iteration of the inner loop), a scale mixing is applied in order to move the low-wavenumber model updates into a new background gradient $\nabla_{\mathbf{b}}\tilde{\Phi}_{\mathbf{mix}}$, and the high-wavenumbers updates into a new perturbation gradient $\nabla_{\tilde{\mathbf{p}}}\tilde{\Phi}_{\mathbf{mix}}$. $\nabla_{\mathbf{b}}\tilde{\Phi}$ is modified by extracting and adding the non-extended part of the perturbation gradient $\nabla_{\tilde{\mathbf{p}}}\tilde{\Phi}_{\mathbf{ne}}$ to the background gradient and by applying a low-wavenumber pass filter,

$$\nabla_{\mathbf{b}}\tilde{\Phi}_{\mathbf{mix}} = \mathbf{F_{low}}\big(\nabla_{\mathbf{b}}\tilde{\Phi} + \nabla_{\tilde{\mathbf{p}}}\tilde{\Phi}_{\mathbf{ne}}\big). \tag{8}$$

where $\mathbf{F_{low}}$ is a low-wavenumber pass filter. In an analogous fashion, we modify the extended perturbation gradient $\nabla_{\tilde{\mathbf{p}}}\tilde{\Phi}$,

$$\nabla_{\tilde{\mathbf{p}}}\tilde{\Phi}_{\mathbf{mix}} = \big(\mathbf{I_d} - \mathbf{F_{low}}\big)\big(\nabla_{\mathbf{b}}\tilde{\Phi} + \nabla_{\tilde{\mathbf{p}}}\tilde{\Phi}_{\mathbf{ne}}\big), \tag{9}$$

where $\mathbf{I_d}$ is the identity operator. Note in equation 9, only the non-extended part of $\nabla_{\tilde{\mathbf{p}}}\tilde{\Phi}$ is modified as the scale mixing does not operate on the extended axes.

At the end of each outer loop, we have two inverted parameters, $\mathbf{b}$ (which contains the lowest wavenumber components) and $\tilde{\mathbf{p}}$ (which contains the highest wavenumber components) that we need to move into one background model $\mathbf{b}$. To do so, we extract the non-extended part of the inverted perturbation $\tilde{\mathbf{p}}$, add it to the inverted background, and apply a low-wavenumber pass filter. The reason for applying this filter is to control and slowly increase the wavenumber content of our inverted model $\mathbf{b}$ because incorrect high-wavenumber updates may affect the convergence efficiency of TFWI. Indeed, the filters' cut-off frequencies (both for the gradients and for $\mathbf{b}$) should be modified with outer loop iterations as we include higher and higher wavenumber components in the background during the inversion. At the end of the TFWI optimization scheme, (1) the inverted model $\mathbf{b}$ should contain all available wavenumbers recoverable from the data, and (2) the data predicted from model $\mathbf{b}$ should match the observed ones.

MODEL EXTENSION FOR COMPLEX WAVEFIELDS

As explained in Almomin (2016), cycle-skipping occurs for FWI (when using gradient-based optimization methods) because the model space is much smaller than the data space, resulting in the averaging and the destructive interference of many data components and the loss of kinematic information in the model space.

Avoiding cycle-skipping in FWI

In order to avoid cycle-skipping issues, the model and the modeling can be modified (e.g., extended) in order to preserve all kinematic information in the data. A nonlinear operator $\mathbf{f}$ with a linearized operator $\mathbf{F}$ (say about model point $\mathbf{m}_0$) satisfies the previous requirement if the following equation holds true for any model point $\mathbf{m}_0$ and any vector $\mathbf{d}$ (Biondi et al., 2016; Almomin, 2016),

$$\mathbf{F}(\mathbf{m}_0)\mathbf{F}^*(\mathbf{m}_0)\mathbf{d} \approx \mathbf{d} \tag{10}$$

In order to better understand the condition expressed in equation 10, we can start

with the following FWI objective function

$$\Phi(\mathbf{m}) = \frac{1}{2}\|\mathbf{f}(\mathbf{m}) - \mathbf{d^{obs}}\|_2^2. \tag{11}$$

Let $\mathbf{m}_0$ be our initial guess for the nonlinear problem. The first gradient is expressed by

$$\nabla\Phi(\mathbf{m_0}) = \mathbf{F}^*(\mathbf{m_0})(\mathbf{f}(\mathbf{m_0}) - \mathbf{d^{obs}}), \tag{12}$$

and the first model update (using steepest descent) is given by

$$\Delta\mathbf{m_0} = -\alpha\nabla\Phi(\mathbf{m_0}). \tag{13}$$

The updated model is given by $\mathbf{m_1} = \mathbf{m_0} + \Delta\mathbf{m_0}$. To avoid cycle-skipping, the predicted data must be "close" to the observed data, so

$$\mathbf{f}(\mathbf{m_1}) = \mathbf{m_0} + \Delta\mathbf{m_0} \approx \mathbf{d^{obs}}. \tag{14}$$

If the linearization holds true, we can write

$$\mathbf{f}(\mathbf{m_1}) \approx \mathbf{f}(\mathbf{m_0}) + \mathbf{F}(\mathbf{m_0})\Delta\mathbf{m_0} \approx \mathbf{d^{obs}}. \tag{15}$$

Therefore, the condition for avoiding cycle-skipping can be re-written as

$$\alpha\mathbf{F}(\mathbf{m_0})\mathbf{F}^*(\mathbf{m_0})(\mathbf{f}(\mathbf{m_0}) - \mathbf{d^{obs}}) \approx (\mathbf{f}(\mathbf{m_0}) - \mathbf{d^{obs}}). \tag{16}$$

equation 16 should be true for any $\mathbf{m_0}$ and any data residual $\mathbf{d} = \mathbf{f}(\mathbf{m_0}) - \mathbf{d^{obs}}$, and is therefore equivalent to equation 10 (up to a scaling factor α).

Optimal model extensions to predict complex waveforms

When our initial model is inaccurate, the condition expressed in equation 10 is not met and we are exposed to cycle-skipping. One way to solve that issue is to extend our linearized Born modeling operator and increase the dimension of the model space (Biondi and Almomin, 2014; Symes, 2008). Common extensions include vertical and horizontal subsurface offsets, and time-lags (Biondi and Almomin, 2014; Yang, 2013; Biondi et al., 1999). It has been shown that for reasonably complex overburdens, these extensions are able to predict data that stay in phase with the observed ones (Biondi and Almomin, 2014). However, wavefields and wavepaths become extremely complex when penetrating salt bodies and reflecting off their boundaries. Even an extended modeling operator might not be able to capture this complexity, which might lead to cycle-skipping.

In this section, we test the validity of equation 10 with various combination of extensions on a model containing a anomaly embedded in a constant velocity background (Figure 13a). The shape of anomaly tries to replicate the type of tortuosity

we might expect at a top-salt interface. We use a wavelet containing energy up to 45 Hz and a finite-difference grid-size of 10 m x 10 m. We place sources and receivers at the surface spaced every 100 m and 10 m, respectively. Data residuals for a source located at $x = 1$ km are shown in Figures 14(a)-(b). The background data are computed using the true model without the anomaly, which only cancels the direct arrivals. Hence, the data residuals contains all the complex reflection events generated from the complex anomaly.

We compute the left side of equation 10 and we compare it to the data residuals (right side of the equation) for various combination of extensions. Our goal is to find a set of extensions for our Born modeling operator such that it satisfies equation 10. Results are shown in Figures 14(a)-(d). From Figures 15(a)-(c), we can see that the non-extended Born modeling operator fails to reconstruct the data residuals, while time-lags, z-offset extensions (and the combination of the two) seem to allow for a better reconstruction. We also observe that the reprojection produces artifacts (in the reconstructed data) that tend to be stronger for the x-offset extension (or combinations of x-offsets extensions with other extensions) (Figures 18, 19, and 21). We are not completely certain of the origin of such artifacts (and why it is stronger for the x-offset extension). However, we believe that it may be caused that the fact that we do not compensate for the illumination, the imprint of wavelet (e.g., the squaring of its amplitude spectrum due to the convolution introduced in the extended Born modeling) when applying a simple adjoint (equation 13). A possible way to test this hypothesis to be to apply an approximated Gauss-Newton step before reprojecting in the data space. Nevertheless, from these results, it seems that using combinations of extensions can potentially be efficient to satisfy the condition expressed in equation 10, even for complex salt bodies.

SUMMARY AND FUTURE WORK

We showed that FWI rapidly fails at recovering large and sharp velocity contrasts, such as the ones encountered in salt basins. In the synthetic examples conducted in this report (which contained noise-free, ultra-low frequency data and ideal acquisition geometries), FWI was not able to converge towards the correct solution. These results led us to pursue the work of Almomin (2016) and understand if and where it fails at inverting for very complex salt boundaries. We are still benchmarking our TFWI code, investigating its optimal parameters (such as the ones used for filtering the gradients and the model updates), and currently testing the algorithm on model containing anomalies with large and sharp velocity contrasts. Future steps include testing TFWI on more realistic examples, such as the one conducted in this report which contains the complex salt structure.

REFERENCES

Almomin, A., 2016, Tomographic full waveform inversion: Stanford University.

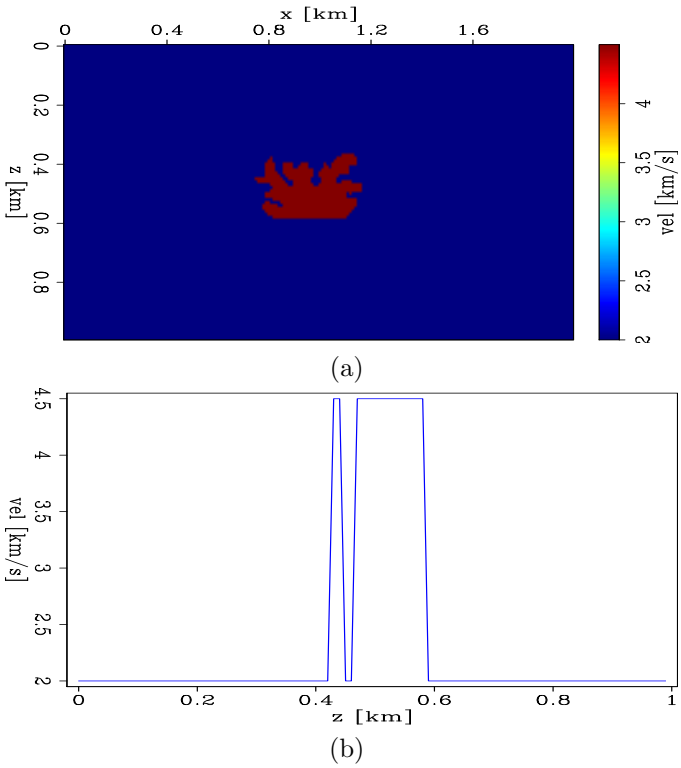

Figure 13: (a) Velocity model containing. (b) velocity profile of the true model extracted at $x = 1$ km. [**CR**]

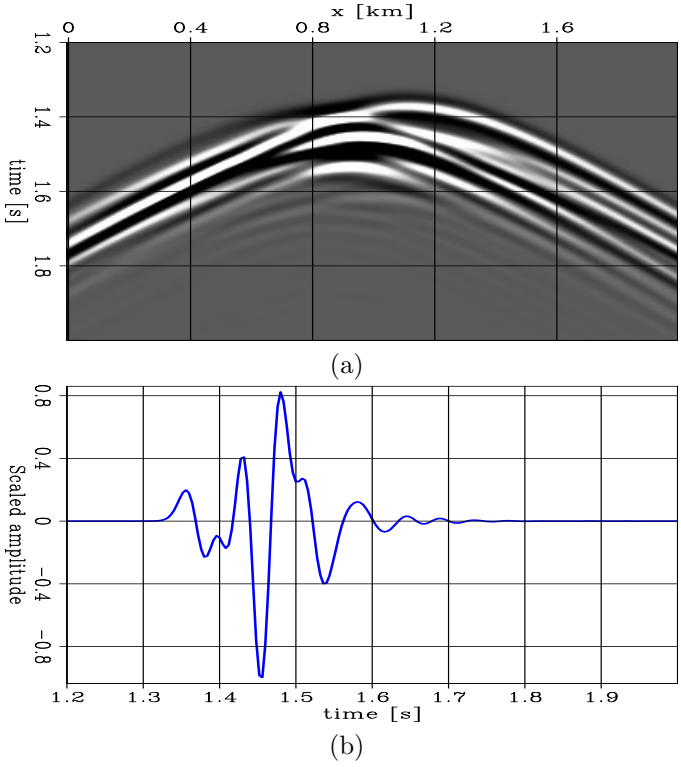

Figure 14: (a) Shot record generated by a source located at $x = 1$ km offset. (b) Trace extracted at $x = 1$ km. [**CR**]

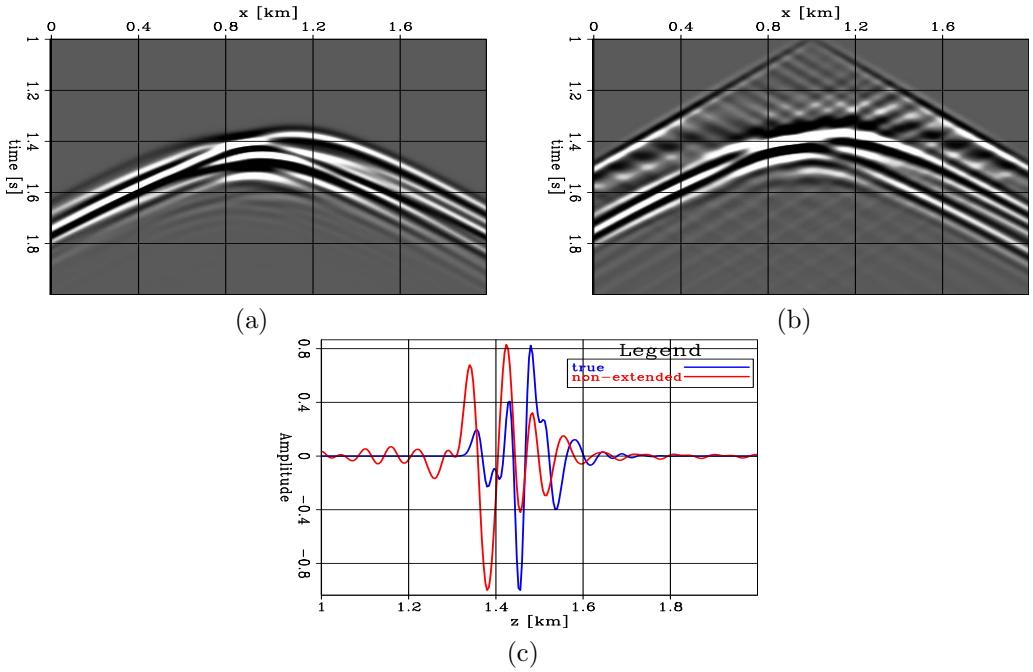

Figure 15: (a) Data residuals. (b) Data residuals after reprojection using a non-extended Born operator. [**CR**]

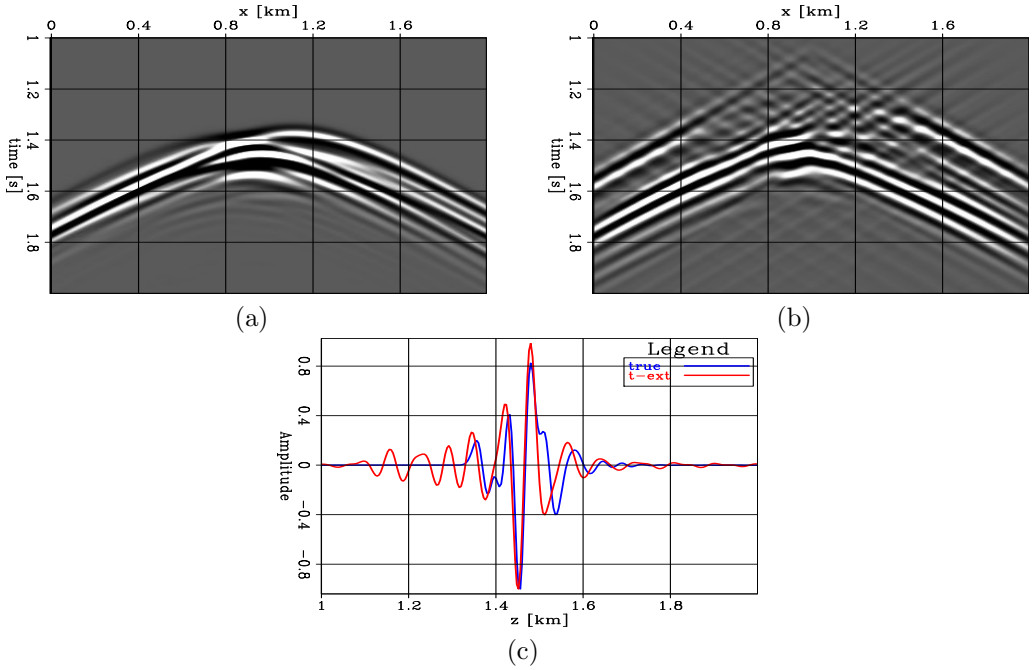

Figure 16: (a) Data residuals. (b) Data residuals after reprojection using a time-lag extended Born operator. [**CR**]

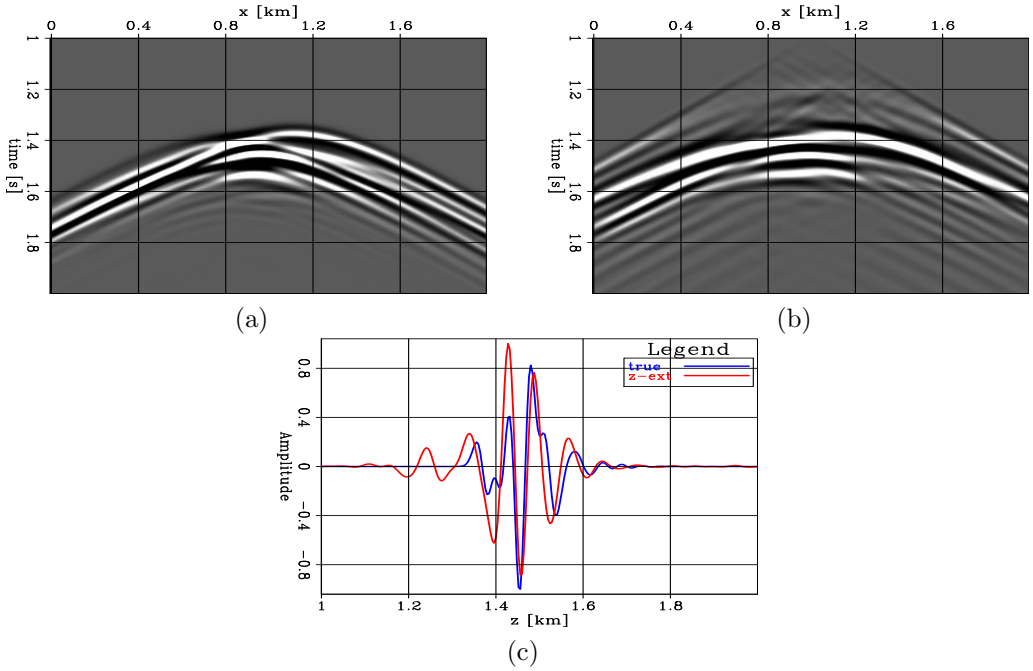

Figure 17: (a) Data residuals. (b) Data residuals after reprojection using a z-offset extended Born operator. [**CR**]

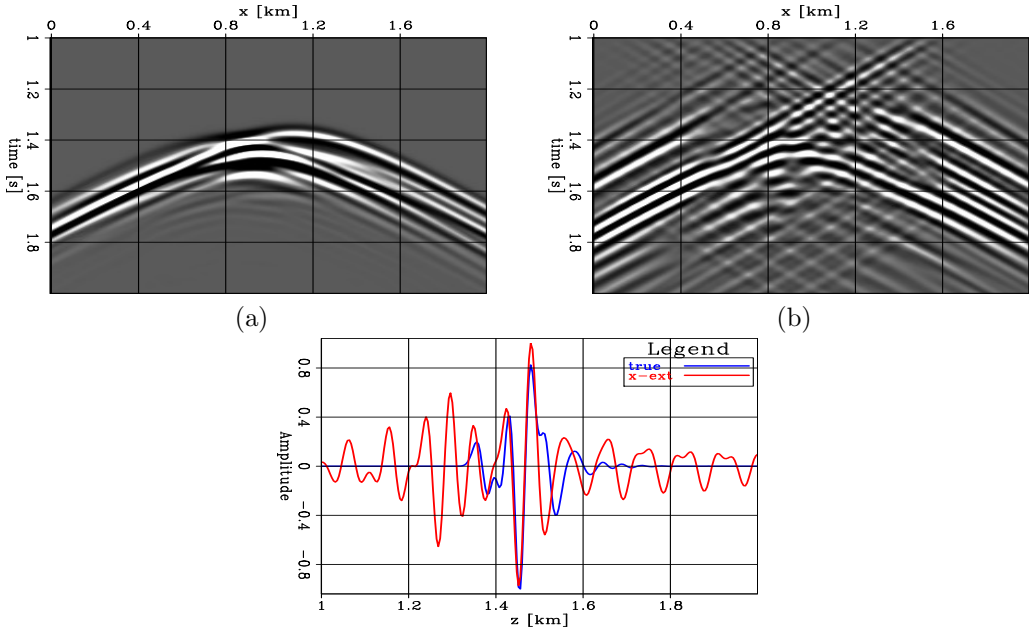

Figure 18: (a) Data residuals. (b) Data residuals after reprojection using a x-offset extended Born operator. [**CR**]

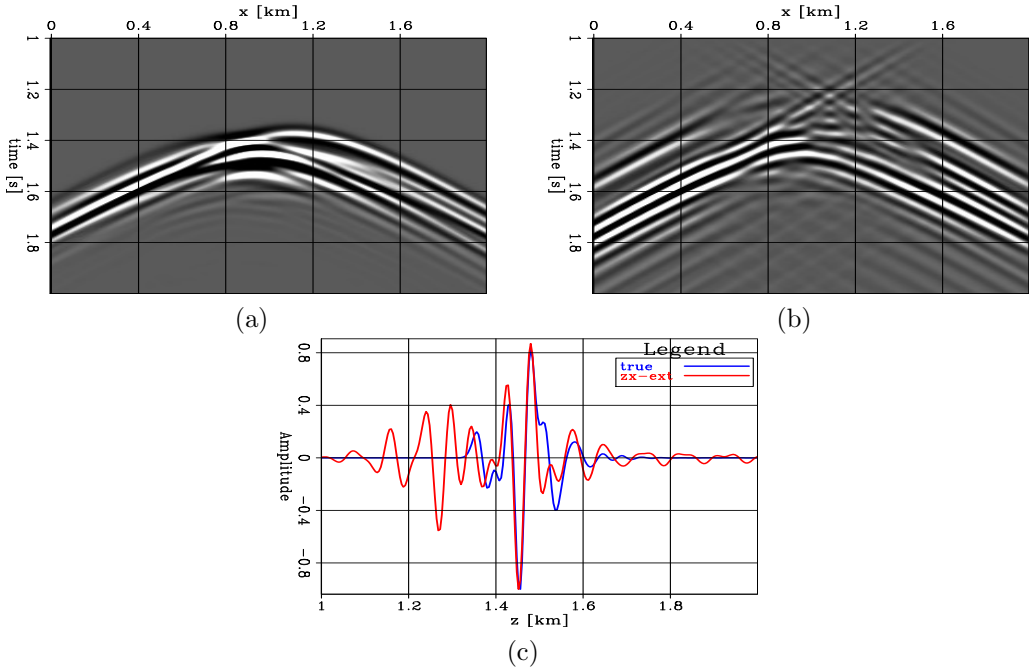

Figure 19: (a) Data residuals. (b) Data residuals after reprojection using a z-offset and x-offset extended Born operator. [**CR**]

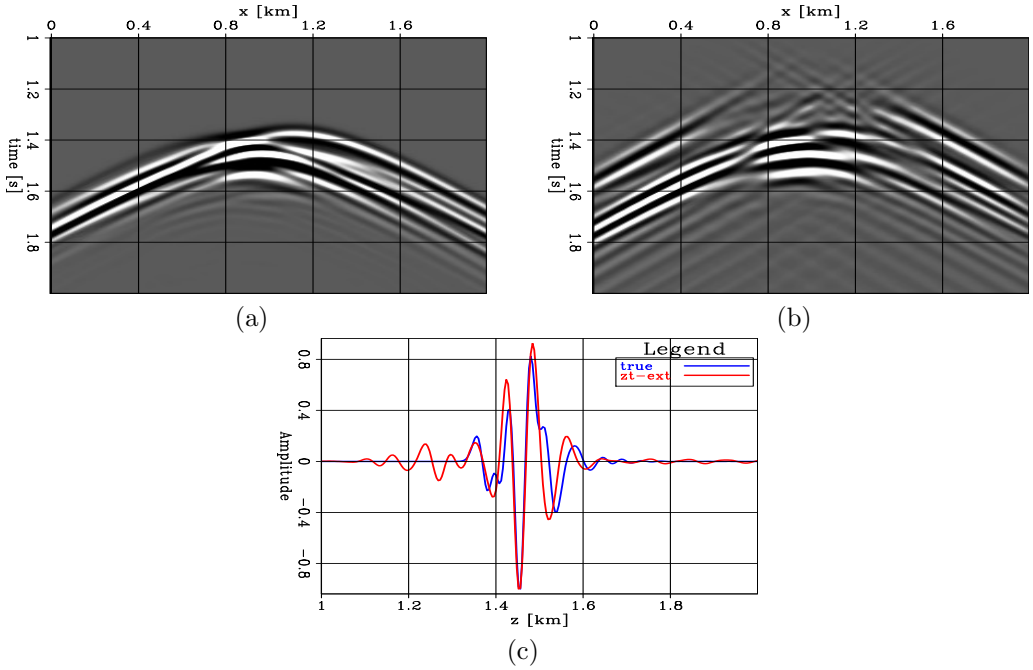

Figure 20: (a) Data residuals. (b) Data residuals after reprojection using a z-offset and time-lag extended Born operator. [**CR**]

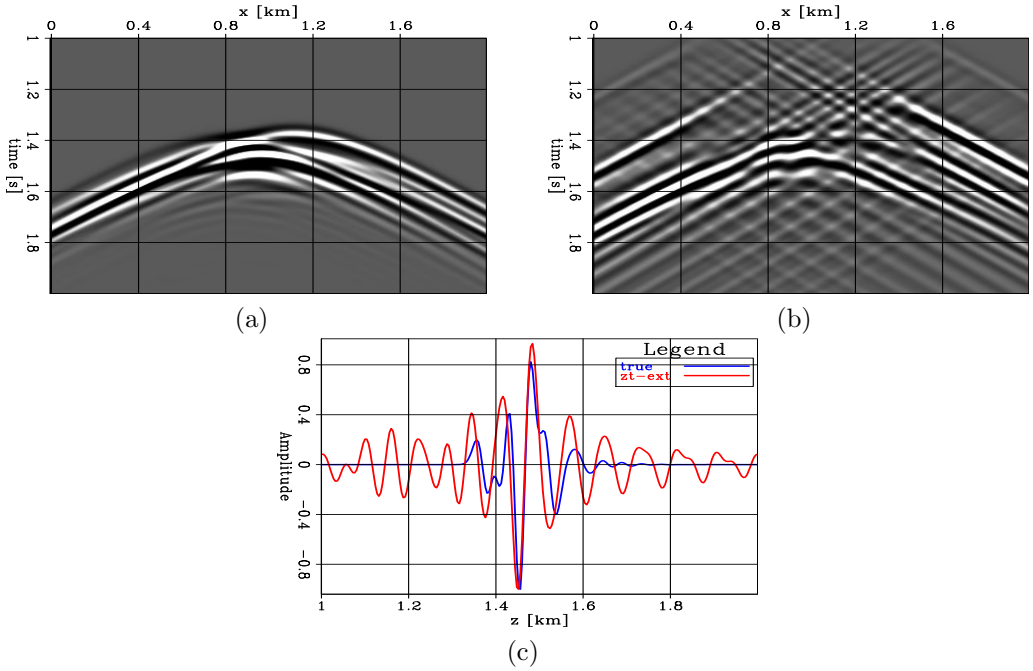

Figure 21: (a) Data residuals. (b) Data residuals after reprojection using all extensions. [**CR**]

Barnier, G. and B. Biondi, 2015, Addressing the effects of inaccurate top-salt delineation on subsalt seismic imaging: SEP-Report, **158**, 67–102.

Biondi, B. and A. Almomin, 2014, Simultaneous inversion of full data bandwidth by tomographic full-waveform inversion: Geophysics, **79**, WA129–WA140.

Biondi, B., R. Sarkar, and J. Jennings, 2016, Solving nonlinear inverse problems by linearized model extension - a survey of possible methods: SEP-Report, **165**, 93–122.

Biondi, B., P. Sava, et al., 1999, Wave-equation migration velocity analysis: 69th Ann. Internat. Mtg Soc. of Expl. Geophys, 1723–1726.

Biondi, E. and G. Barnier, 2017, A flexible out-of-core solver for linear/non-linear problems: SEP-Report, **168**.

Bunks, C., F. M. Saleck, S. Zaleski, and G. Chavent, 1995, Multiscale seismic waveform inversion: Geophysics, **60**, 1457–1473.

Clapp, R. G., 2014, Synthetic model building using a simplified basin modeling approach: SEP-Report, **155**, 145–152.

Etgen, J. T., I. Ahmed, M. Zhou, et al., 2014a, Seismic adaptive optics: Presented at the 2014 SEG Annual Meeting.

Etgen, J. T., C. Chu, T. Yang, M. Vyas, et al., 2014b, Adaptive image focusing: Presented at the 2014 SEG Annual Meeting.

Lewis, W., B. Starr, and D. Vigh, 2012, A level set approach to salt geometry inversion in full-waveform inversion, *in* SEG Technical Program Expanded Abstracts 2012, 1–5, Society of Exploration Geophysicists.

Mora, P., 1989, Inversion= migration+ tomography: Geophysics, **54**, 1575–1586.

Shen, X., 2014, Early-arrival wavefrom inversion for near-surface velocity estimation: Stanford University.

Symes, W. W., 2008, Migration velocity analysis and waveform inversion: Geophysical prospecting, **56**, 765–790.

Wang, K., B. Deng, Z. Zhang, L. Hu, and Y. Huang, 2015, Top of salt impact on full waveform inversion sediment velocity update, *in* SEG Technical Program Expanded Abstracts 2015, 1064–1069, Society of Exploration Geophysicists.

Williamson, P., C. Rivera, and K. Mansoor, 2016, Acoustic fwi applied to subsalt imaging: an illuminating case study from offshore angola, *in* SEG Technical Program Expanded Abstracts 2016, 4896–4900, Society of Exploration Geophysicists.

Yang, T., 2013, Wavefield tomography using extended images: Colorado School of Mines.